Dependency of the apparent contact angle on nonisothermal conditions

5 AUTHORS, INCLUDING:

Jens Gerstmann
German Aerospace Center (DLR)
22 PUBLICATIONS   52 CITATIONS

SEE PROFILE

Michael Dreyer
Universität Bremen
168 PUBLICATIONS   834 CITATIONS

SEE PROFILE

Dependency of the apparent contact angle on nonisothermal conditions

Rolf Krahl, Jens Gerstmann, Philipp Behruzi, Eberhard Bänsch, and Michael E. Dreyer
Applied Mathematics III, University Erlangen-Nuremberg, Haberstr. 2, Erlangen 91058, Germany

The dynamic behavior of liquids in partly filled containers is influenced to a large extend by the angle between the gas-liquid phase boundary and the solid container wall at the contact line. This contact angle in turn is influenced by nonisothermal conditions. In the case of a cold liquid meniscus spreading over a hot solid wall, the contact angle apparently becomes significantly larger. In this paper we want to establish a quantitative equation for this enlargement, both from experimental and numerical data. Our findings can be used to build a subgrid model for computations, where the resolution is not sufficient to resolve the boundary layers. This might be the case for large containers which are exposed to low accelerations and where the contact angle boundary condition determines the position of the free surface. These types of computation are performed, for example, to solve propellant management problems in launcher and satellite tanks. In this application, the knowledge of the position of the free surface is very important for the withdrawal of liquid and the calculation of heat and mass transfer. © *2008 American Institute of Physics*. [DOI: 10.1063/1.2899641]

I. INTRODUCTION

The prediction of the dynamic behavior of liquids in partly filled containers is still a challenging task, in particular, in situations with a small Bond number, when capillary forces become important. This is, for instance, the case for the management of cryogenic propellants in tanks of space vehicles. Examples of corresponding space missions are the following:

- Multiboost missions for the deployment of multiple satellites where the upper stages of the launcher perform ballistic phases with variable duration from seconds to hours.
- Missions with delayed engine ignitions. Such missions are carried out for example for extraterrestrial missions such as the Rosetta space probe; see Ref. [1].
- Missions to Moon and Mars.

One important parameter for the behavior of those liquids is the angle between the gas-liquid phase boundary and the solid container wall at the contact line. It determines the shape of the free surface in the tanks, and thus the position of the liquid bulk itself. The knowledge of the liquid distribution is important for the withdrawal of liquid from the tank as well as for the prediction of the heat and mass transfer to keep the tank pressure within its accepted boundaries. The contact angle in turn is influenced by nonisothermal conditions. It apparently becomes larger for a cold liquid meniscus spreading over a hot wall, see Ref. [2]. A similar effect has been observed by Ehrhard and Davis,[3] studying the spreading of liquid drops on heated horizontal surfaces. In this case, the thermocapillary force caused by the temperature gradient between the cold liquid and the hot plate substantially retards the spreading, which is similar to the increase of the contact angle.

Liquids with a static contact angle of zero would spread to infinity. If a temperature gradient exists and a thermocap-illary flow is created, the drop will spread to a finite distance only, thus the effective contact angle is increased. This numerically predicted behavior was later confirmed by Ehrhard[4] in a series of laboratory experiments with perfectly and partially wetting liquids. Anderson *et al.*[5] extended this work to volatile liquid droplets and took into account the effect of evaporation from the drop surface. However, these papers did not focus on the contact angle behavior in detail and they did not provide a correlation for the effective contact angle as a function of the applicable dimensionless numbers for thermocapillary motion. We could not find papers that deliver a general correlations for the dependence of the contact angle on temperature gradients between liquid and solid. To formulate such a correlation is the aim of this paper.

In Ref. [6] we were able to reproduce the effect of an increasing *effective* contact angle in numerical simulations at least qualitatively *without* modifying the static contact angle that was prescribed as boundary condition, only considering the thermocapillary convection induced by the temperature gradient at the phase boundary. These results indicate that this effect does not require a sophisticated contact angle model in numerical simulations, provided that the computational grid is fine enough to resolve the small scale effects close to the contact line. However, such a fine grid is unaffordable in simulations performed with commercial CFD codes for large scale computations to design tanks of space vehicles in an efficient manner. In this context, an accurate evaluation of the wetted tank surface is of importance, since it influences the heat flux into the tank as well as the heat distribution in the liquid with respect to time. For the standard liquids used in space applications (e.g., hydrazine, MMH, N_2O_4, LH_2, LOX), the static contact angle is about zero under isothermal conditions leading to a total wetting of the tank surfaces. This may, however, not be true under nonisothermal conditions, especially for cryogenic liquids. Heat fluxes into the tank will force larger macroscopic static contact angles greater than zero. Hence there is a need to
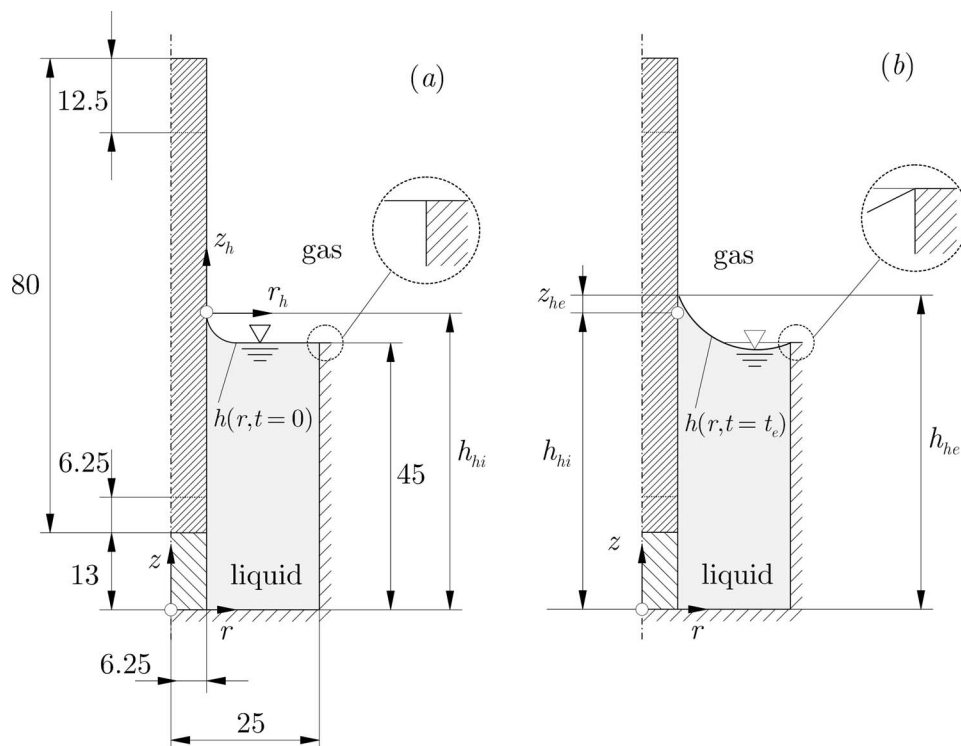
FIG. 1. (a) Geometry and initial free surface configuration at normal gravity condition. Dimensions in mm. (b) Free surface configuration at compensated gravity conditions.

formulate and to verify macroscopic boundary conditions describing the small scale effects that cannot be resolved on the coarse numerical grids used in the industrial practice.

Thus the aim of the present paper is to establish a quantitative estimation of the enlargement of the apparent contact angle caused by nonisothermal conditions. To this end, both experiments and numerical simulations in an annular gap have been performed. Related to the somewhat cylindrical geometries of spacecraft tanks, former tests have been performed mainly in a right circular cylindrical container. Besides the problem of the application of a known temperature boundary condition on the *inner* wall of the cylinder, the observation of the contact line is difficult unless liquids of the same index of refraction as the transparent container material are used, see Michaelis *et al.*[7] and Dreyer.[8] These liquids do not lead to the right order of magnitude of the corresponding dimensionless numbers to make this work applicable to situations in propellant tanks. Thus, an annular gap geometry with a low viscosity liquid has been chosen to achieve a better observation in contrast to experiments in a right circular container.

Steady thermocapillary convection in an annular gap geometry has been studied by Kamotani *et al.*[9] in the Surface Tension Driven Convection Experiment-2 (STDCE-2) aboard the USML-2 Spacelab in 1995. The main focus was the observation of the onset of an oscillatory mode of the thermocapillary convection. The experimental technique did not allow us to visualize and to measure the free surface shape in the vicinity of the contact line nor the contact angle itself. Furthermore, a steady, fully developed flow field was achieved by heating the liquid with a central rod heater (like

in our case) and cooling the walls to a constant temperature. Thus the results cannot be used for the purpose of this paper to derive a correlation for the effective contact angle, but the computed flow and temperature fields are similar to ours and the scaling arguments are very helpful to find the right dimensionless numbers. This is outlined in the next sections.

II. PHYSICAL DESCRIPTION AND MATHEMATICAL MODEL

A. Physical description

Consider an annular gap, partly filled with liquid, around a cartridge heater, see Fig. 1. The contact line at the outer wall was pinned by a sharp edge of the vessel wall. The inner contact line was free to move up and down the wall at the heater. The contact angle at the inner wall is to be observed.

Initially, the liquid was in the isothermal 1 *g* equilibrium configuration. The free liquid surface was characterized by a flat shape with a small meniscus at the inner wall. The filling height of the liquid was adjusted such that the liquid surface forms a 90° contact angle at the outer wall. Experimentally, a step reduction in gravity was obtained by the release of a drop capsule in the drop tower facility of the Center of Applied Space Technology and Microgravity in Bremen. A capillary driven reorientation of the liquid to the new 0 *g* equilibrium position was then established through a damped oscillation.

Shortly before the transition to reduced gravity, the heater was switched on and the temperature raises linearly in time at the inner wall. The temperature gradient induced a Marangoni stress at the phase boundary, exciting a flow in

TABLE I. Definition of the dimensionless numbers. ρ is the density of the liquid, μ the dynamic viscosity, σ the surface tension, σ_T the variation of surface tension with temperature, c_p the specific heat capacity, λ the heat conductivity, and β_T the thermal expansion coefficient. The characteristic values are the width of the annular gap L, the characteristic velocity U as defined in Eq. (8), the difference between the wall temperature at the heater and the initial temperature of the fluid Θ, and the external acceleration g. g is the earth gravity initially and drops to zero shortly after the beginning of the experiment.

$\text{Bo} = \dfrac{\rho g L^2}{\sigma}$	Bond number
$\text{Oh} = \dfrac{\mu}{\sqrt{\rho \sigma L}}$	Ohnesorge number
$\text{Pr} = \dfrac{\mu c_p}{\lambda}$	Prandtl number
$\text{Ra} = \dfrac{g \rho^2 \beta_T \Theta L^3 c_p}{\lambda \mu}$	Rayleigh number
$\text{Re} = \dfrac{\rho U L}{\mu}$	Reynolds number
$\text{Re}_M = \dfrac{\rho \sigma_T \Theta L}{\mu^2}$	Thermocapillary Reynolds number
$\text{We} = \dfrac{\rho U^2 L}{\sigma}$	Weber number
$\text{We}_M = \dfrac{\rho U^2 L}{\sigma_T \Theta}$	Thermocapillary Weber number

the liquid and a deformation of the free surface. This deformation superimposed the reorientation of the surface due to the drop in gravity. In the numerical simulations in Sec. IV, we also consider the case without reorientation, where we started in the isothermal $0g$ equilibrium configuration from the beginning. We denote by ϑ_l the initial temperature of the liquid and by ϑ_u the maximal temperature at the heater at the end of the experiment.

B. Mathematical model and dimensionless numbers

We assume the flow in the bulk of the liquid phase to be governed by the incompressible Navier–Stokes equations and to have an advection-diffusion equation for the heat transport, which read in dimensionless form as

$$\partial_t \mathbf{u} + \mathbf{u} \cdot \nabla \mathbf{u} - \frac{1}{\text{Re}} \Delta \mathbf{u} + \nabla p = \frac{\text{Bo}}{\text{We}} \mathbf{e}_g - \frac{\text{Ra}}{\text{PrRe}^2} \vartheta \mathbf{e}_g, \qquad (1)$$

$$\nabla \cdot \mathbf{u} = 0, \qquad (2)$$

$$\partial_t \vartheta + \mathbf{u} \cdot \nabla \vartheta - \frac{1}{\text{PrRe}} \Delta \vartheta = 0, \qquad (3)$$

where $\mathbf{u}$ is the liquid velocity, p the pressure, ϑ the temperature, and $\mathbf{e}_g$ is the unit vector in the direction of the external acceleration. The definitions of the dimensionless numbers are given in Table I.

The motion of the gas-liquid phase boundary is assumed to follow the flow that is, the normal velocity of the free surface u_Γ is equal to the normal component of the liquid velocity,

$$u_\Gamma = \mathbf{u} \cdot \mathbf{n}. \qquad (4)$$

Furthermore, we assume the following balance of forces to hold at the boundary:

$$\mathbf{T}\mathbf{n} = \frac{1}{\text{We}} \kappa \mathbf{n} - \frac{1}{\text{We}_M} \nabla_S \vartheta, \qquad (5)$$

where $\mathbf{T} = -p\mathbf{I} + (1/\text{Re})[\nabla \mathbf{u} + (\nabla \mathbf{u})^T]$ is the dimensionless stress tensor, $\mathbf{n}$ the unit normal vector to the free surface, pointing in the direction of the gaseous phase, κ the curvature of the free surface, and $\nabla_S \vartheta$ the gradient of the temperature along the free surface. We do not consider any influences from the gaseous phase on the problem, that is, we neglect the stresses exerted by the gas on the phase boundary, as well as any mass and heat transfer. Note that in the full model of the two phase flow, the pressure appears only as a gradient in the bulk of the phases and as a jump term at the phase boundary, and thus, it is determined only up to an additive constant. Assuming homogeneity in the gas phase, we may therefore normalize it to zero at the gas side of the phase boundary. That is why we may neglect also the pressure from the gas side.

As boundary condition for the shape of the free surface we assume a fixed contact line at the sharp edge in the outer wall. At the inner wall, the static contact angle γ_s between the liquid surface and the wall is prescribed.

At the walls, we assume to have no slip,

$$\mathbf{u} = 0. \qquad (6)$$

However, the combination of the no-slip condition at the wall [Eq. (6)] and the kinematic boundary condition (4) leads to a stress singularity at the contact line. This is a result of the modeling of the surface as a mathematical one having a sharp contact line on the wall. From physical evidence it is known that the surface extends over some molecular diameters of the matter involved, and that adsorbed films on the wall exist ahead of this mathematical contact line, in particular, for perfectly wetting liquids as in our case, or that other mechanisms such as a rolling motion circumvent the moving contact line problem, see Ref. 10. As a remedy for the artificial stress singularity, a Navier slip condition has been introduced (as already discussed by Lamb in Ref. 11, pp. 576 and 586). Modern numerical methods allow us to change the boundary condition at the wall from a slip condition directly at the contact line to a no-slip condition for a small length l_s (as discussed in Sec. IV C). This length shall not be confused with the extrapolation length used in the Navier slip condition. The choice of the length l_s is somewhat arbitrary and the influence of its size on the results is discussed in Sec. IV E.

We follow the approach proposed by Ostrach in Ref. 12 for the scaling of a thermocapillary flow. According to this paper, the flow has a boundary layer character if

$$\text{Re} \left(\frac{D}{L} \right)^2 \gg 1, \qquad (7)$$

where the Reynolds number is defined via a characteristic velocity $\sigma_T \Theta D / \mu L$ resulting in $\text{Re} = \sigma_T \Theta D / \mu \nu$, where ν is the kinematic viscosity. Since the value of the product of the

TABLE II. Properties of HFE-7100 at a temperature of 25 °C.

σ (mN/m)	σ_T [mN/(m K)]	ρ (kg/m^3)	ν (mm^2/s)	c_p [J/(kg K)]	λ [W/(m K)]
13.6	0.12	1517	0.38	1180	0.069

thermocapillary Reynolds number Re_M times the aspect ratio was always larger than 10^5 in our experiments, this criterion is completely fulfilled. Therefore, we may choose the width of the annular gap L as the characteristic length and need not to consider the aspect ratio of liquid depth D to gap width L, in our case $45/18.75 \text{ mm} = 2.4$. The appropriate thermocapillary Reynolds number is then the one given in Table I and the characteristic velocity scale is

$$U = \left(\frac{\sigma_T^2 \Theta^2}{\rho^2 \nu L} \right)^{1/3}. \tag{8}$$

This is also confirmed by computations of Kamotani *et al.*[13] for a similar configuration but a fixed contact angle of 90°.

Using this scaling, the dimensionless factors appearing in Eq. (1)–(5) can be rewritten as

$$\frac{1}{\mathrm{Re}} = \mathrm{Re}_M^{-2/3}, \tag{9}$$

$$\frac{\mathrm{Bo}}{\mathrm{We}} = \mathrm{Bo}\frac{\mathrm{We}_M}{\mathrm{We}}\mathrm{Re}_M^{-1/3}, \tag{10}$$

$$\frac{\mathrm{Ra}}{\mathrm{Pr}\mathrm{Re}^2} = \frac{\mathrm{Ra}}{\mathrm{Pr}}\mathrm{Re}_M^{-4/3}, \tag{11}$$

$$\frac{1}{\mathrm{Pr}\mathrm{Re}} = \frac{1}{\mathrm{Pr}}\mathrm{Re}_M^{-2/3}, \tag{12}$$

$$\frac{1}{\mathrm{We}} = \frac{\mathrm{We}_M}{\mathrm{We}}\mathrm{Re}_M^{-1/3}, \tag{13}$$

$$\frac{1}{\mathrm{We}_M} = \mathrm{Re}_M^{-1/3}. \tag{14}$$

In our case Ba and Ra drop to zero shortly after the beginning of the experiment. Thus, the scaling yields the Reynolds–Marangoni number Re_M as well as the ratio $\mathrm{We}/\mathrm{We}_M$ of thermocapillary Weber and Weber number as the relevant characteristic numbers.

Note that the Reynolds–Marangoni number could also be written as a combination of $\mathrm{We}/\mathrm{We}_M$ and the Ohnesorge number,

$$\mathrm{Re}_M = \frac{1}{\mathrm{Oh}^2}\frac{\mathrm{We}}{\mathrm{We}_M}. \tag{15}$$

In the experiments, the Fluorinert HFE-7100 has been used as test liquid. Its properties at a temperature of 25 °C are listed in Table II. The resulting Ohnesorge number is $\mathrm{Oh} = 9.3 \times 10^{-4}$, the Prandtl number is $\mathrm{Pr} = 9.86$, and the initial Bond number is $\mathrm{Bo} = 385$. Re, Re_M, We, and We_M depend on the temperature difference Θ between the heater surface

and the liquid. Since the Ohnesorge number was kept constant in the annular gap experiment, the temperature depending contact line behavior depends solely on

$$\frac{\mathrm{We}}{\mathrm{We}_M} = \frac{\sigma_T \Theta}{\sigma}. \tag{16}$$

Thus the given correlation with respect to $\mathrm{We}/\mathrm{We}_M$ is only valid for this particular value of the Ohnesorge number and the corresponding range of the Re_M number $8.1 \times 10^4 < \mathrm{Re}_M < 4.6 \times 10^5$. The range of Marangoni numbers Ma with $\mathrm{Ma} = \mathrm{Re}_M\mathrm{Pr}$ would correspond to $8.0 \times 10^5 < \mathrm{Ma} < 4.5 \times 10^6$.

The shape of the isothermal equilibrium surface for any given Bond number (and, in particular, the isothermal equilibrium surface in the absence of external acceleration, $\mathrm{Bo} = 0$) is characterized by setting $\mathbf{u} = 0$ and $\vartheta = 0$ in Eqs. (1)–(5), and thus obtaining the Young–Laplace equation

$$\kappa = \mathrm{Bo}z - c, \tag{17}$$

where κ is the curvature of the free surface, z the vertical coordinate, and c a constant depending on the filling height of the liquid. This constant has been determined numerically in the following way: In a first step, the liquid volume has been calculated by solving Eq. (17) with $\mathrm{Bo} = 385$ and $c = \mathrm{Bo}z_w$, where $z_w = 2.4$ is the dimensionless height of the edge in the vessel wall. This results in the 1 g equilibrium surface that was the initial configuration in the experiments. The 0 g configuration for $\mathrm{Bo} = 0$ was then obtained in an iterative loop with an initial value of $c = 0$: Solving Eq. (17), calculating the error in the liquid volume for this solution and incrementing c by this error. This scheme converges pretty fast toward a surface with the correct volume.

The goal of this paper was to study and quantify the angle between the liquid surface and the wall very close to the contact line. In the experiments, we cannot measure this angle directly at the contact line, since this by definition involves the slope of the surface, which in turn can only be measured at some distance from the wall. The smallest distance is limited by the optical resolution of the recording devices.

In the numerical simulations with the software FLOW-3D, the situation is similar, since here, the free surface is only implicitly defined by the filling height of the grid cells. With our software NAVIER used in the present paper, we have an explicit parametrization of the free surface and therefore we could in principle measure the contact angle directly at the wall. However, for NAVIER we prescribe this angle as a boundary condition (see Sec. IV), so that the impact of the nonisothermal conditions on the shape of the surface can only be seen at some distance from the wall.

Therefore we define, what we will call the *apparent contact angle* γ_{dl} hereafter, to be the slope of the free surface at a certain distance $r_l = 0.14$ mm from the wall. Note that also in the isothermal case we have $\gamma_{\mathrm{dl}} > \gamma_s$ due to the curvature of the free surface. To account for this, we define a reference contact angle γ_0 to be the slope of the free surface at r_l under isothermal conditions in the 0 g equilibrium shape, see Fig. 2(b). This equilibrium shape can be computed by solving the
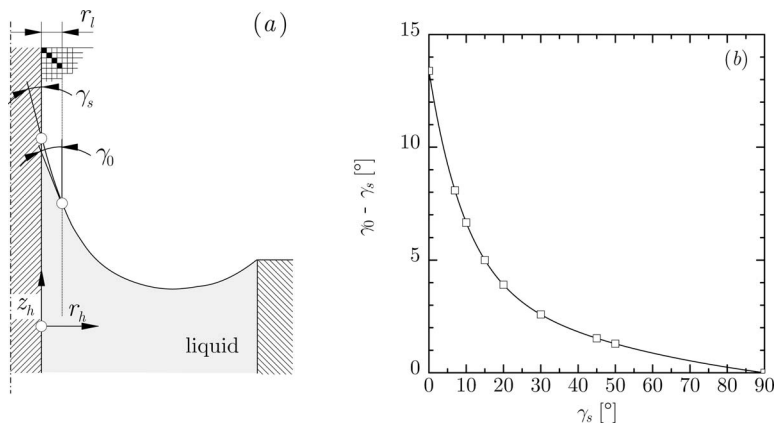
FIG. 2. (a) Shape of free surface at microgravity conditions. The static contact angle (γ_s) at the heater wall differs from the contact angle (γ_0) at a distance of r_l =0.14 mm from the wall. The difference decreases with increasing γ_s as shown in (b).

Young–Laplace equation (17). For a fully wetting fluid, characterized by $\gamma_s = 0°$, we have $\gamma_0 = 13.3°$. Then we define the enlargement γ_{shift} of the apparent contact angle by

$$\gamma_{shift} := \gamma_{dl} - \gamma_0. \tag{18}$$

III. EXPERIMENTS IN THE DROP TOWER

Experiments have been performed in the Drop Tower Facility in Bremen. The geometric setup was the one described in Sec. II A.

A. Experimental setup

The experimental setup consisted of the circular cylinder manufactured from a solid polymethyl methacrylate cube, the cartridge heater placed along the symmetry axis, the test liquid, the temperature measurement system, pressure measurement, the high speed digital recording system, and background illumination device. The experimental setup was integrated in a drop capsule.

Above the edge in the outer wall, the container cross section changed from cylindrical to quadratic. Thus in com-

bination with the outer cubic form of the test vessel optical disturbances resulting from light refraction could be avoided and an undisturbed view on the contact line at the cartridge heater was feasible. This allowed the evaluation of the dynamic contact angle and the contact line coordinate in dependence on the nonisothermal boundary condition. The cartridge heater was commercially available and manufactured by Friedrich Freek GmbH, Germany. The diameter was 12.5 mm, the length was 80 mm, and the maximum heating power was 200 W which was varied in the experiment series. In order to avoid light reflection, the heater surface was varnished with beamless black paint.

Due to the closed test section a defined state of the gas in the void region was adjustable. The inert gas argon 6.0 was used as filling for the void region above the test liquid. The test vessel was filled with the test liquid HFE-7100 up to the edge of the interior side of the vessel wall. The Fluorinert HFE-7100 was manufactured by 3M.

The reorientation process was recorded by a high speed digital recording system. Two charge coupled device cameras with a resolution of 512×480 pixel were used to record the liquid motion with a frame rate of 250 frames/s. A de-
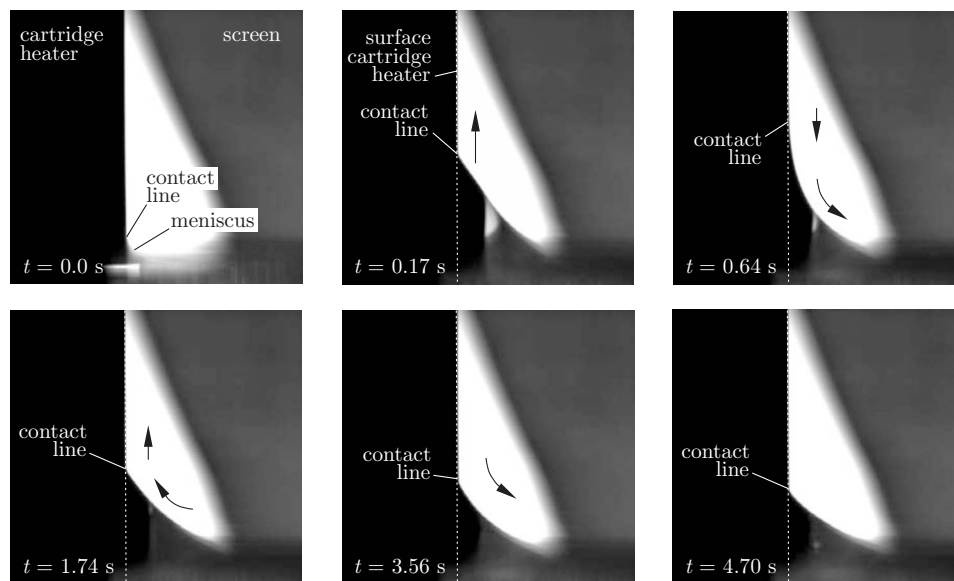

FIG. 3. Sequence of video frames (512×480 pixel; 14.3×13.4 mm) from nonisothermal experiment 14.

TABLE III. Parameters of drop tests.

No.	P (W)	p (hPa)	t_h (s)	ϑ_l (°C)	ϑ_u (°C)	Θ (K)	We/We$_M$ (−)	γ_{dl} (°)
9	75	994	−1.14	23.9	43.0	19.1	0.17	29
10	30	1018	−1.29	24.5	32.5	7.9	0.07	22
11	73	1017	−1.11	24.3	42.9	18.6	0.16	28
13	31	999	−1.32	23.0	31.1	8.1	0.07	22
14	201	1975	−0.16	22.7	66.9	44.3	0.38	42
15	207	1975	−0.17	23.2	67.6	44.4	0.39	42
16	133	2001	−0.38	23.8	53.5	29.7	0.26	35
17	133	2018	−0.33	23.5	53.0	29.4	0.26	33
19	164	1998	−0.37	22.3	59.4	37.2	0.32	39
20	165	2008	−0.38	22.3	59.8	37.5	0.32	40
21	106	1995	−0.18	22.8	45.7	22.9	0.20	31

tailed view of the contact line region at the heater with a pixel resolution of about 28 μm/pixel and a total view with a pixel resolution of about 120 μm/pixel were adjusted (Fig. 3).

The temperature measurement was realized by six copper constantan thermocouples (Tc1–Tc6). The wire diameter was 0.13 mm and the response time was 0.04 s. Four thermocouples were placed on the cartridge heater (Tc1–Tc4). The thermocouples were embedded in the heater surface. The thermocouples Tc1 and Tc2 were below the liquid interface, whereas the thermocouples Tc3 and Tc4 were above. The fifth thermocouple Tc5 was placed inside the liquid, whereas the sixth thermocouple Tc6 was placed in the void region above the liquid interface. The pressure was measured by a pressure sensor manufactured by Sensotec model TJE. The measurement range was 0–2 bars with 0.1% accuracy.

B. Parameter range

To investigate the influence of the thermal boundary condition on the apparent dynamic contact angle, the ratio We/We$_M$ of thermocapillary Weber and Weber number was varied by changing the heating power of the cartridge heater.

The parameter are listed in Table III. The temperature increased linearly with time due to the constant heating power during the experiment.

The temperature difference Θ for calculating the We/We$_M$ was specified by the difference between the initial temperature at the heater surface and the temperature at the heater surface at the end of the experiment 4.72 s after the release of the capsule. The obtained value was related to the mean contact angle at the end of the experiment. We/We$_M$ was varied in the range of 0–0.34 by varying the heater power in range of 0–200 W, resulting in an increase of the heater temperature within the experiment time between 0 and 44.4 K.

Due to the high Prandtl number of about Pr=9.9 the thermal boundary layer was small in comparison to the viscous boundary layer. The Bond number and the Rayleigh number were zero during the microgravity time. The properties of the test liquid were calculated based on the initial heater temperature. The local change of the properties due to the temperature increase on the heater wall was not considered.
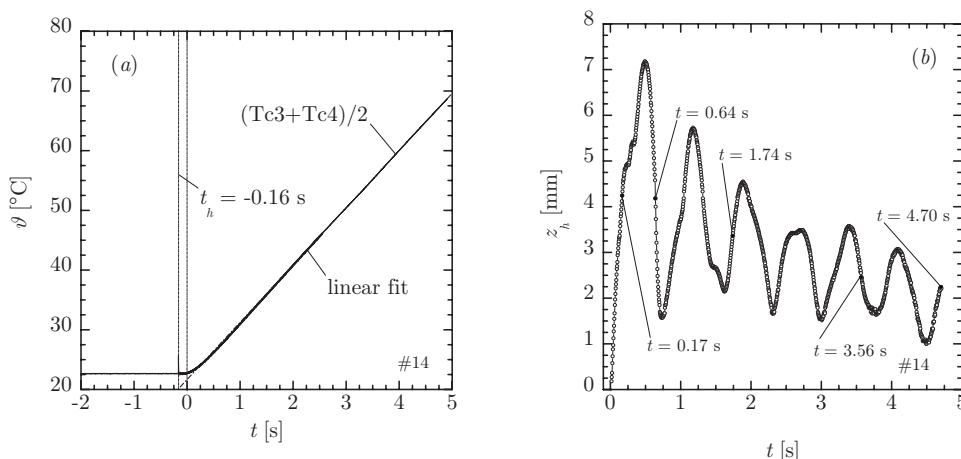

FIG. 4. (a) Temperature evolution on the heater surface vs time. Tc3 and Tc4 are thermocouples located at the heater surface above the liquid interface. (b) Apparent contact line coordinate vs time (time label compare Fig. 3).
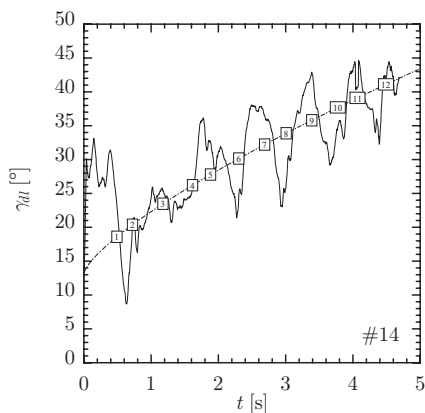
FIG. 5. Apparent dynamic contact angle γ_{dl} vs time. The enumeration of the data points labels the apparent static contact angle at the turning points of the contact line oscillation.

FIG. 6. Final mean apparent dynamic contact angle vs final We/We_M for different experiments.

C. Data evaluation

The commercial software program MATLAB was used for digital image processing for the detection of the liquid interface on the pictures from the detailed view after the experiment. Due to the backlight illumination a total reflection at the liquid/gas interface occurred, where a maximum gradient from a bright region to a dark region appeared. The location of the maximum gradient defined the position of the liquid interface.

In the case of low contact angle the detection of the contact line position as well as the determination of the contact angle direct at the heater surface was difficult and deficient. Thus the contact line behavior and the dynamic contact angle behavior were evaluated at a certain distance r_l =5 pixels from the heater wall. The value of r_l in the series of experiments was of about 0.14 mm. The contact angle γ_{dl} was determined by calculating the gradient of the surface contour at the distance r_l.

The contact angle γ_s at the heater wall differed from the contact angle γ_{dl} at a certain distance r_l from the wall, see Fig. 2(a) and the discussion in Sec. II B.

D. Experimental accuracy

Temperature variances along the heated part of the heater wall were within 5%. The thermocouples had an accuracy of $\pm 0.5\,^\circ$C and a response time of 0.04 s. The accuracy of the routine for detecting the interface contour was on the order of ± 2 pixel. The error of the determined contact angle was below $\pm 5°$. The inaccuracy with regard to the experiment time depended on the recording frequency of 250 frames/s, resulting in an error of the order of ± 2 images, corresponding to 0.008 s.

E. Results

A typical temperature evolution recorded by the thermocouples Tc3 and Tc4 are shown in Fig. 4(a). The temperature at the heater surface increased with a short delay approximately linear in time. The heating of the cartridge heater was
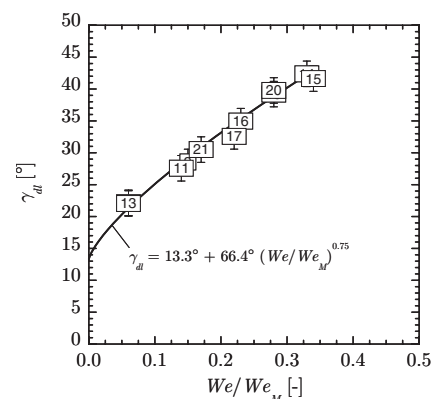
started at t_h=−0.16 s (in dimensional units) prior to the drop. Thus the linear fit of the temperature originates at $t \approx 0$ s.

The corresponding reorientation behavior of the contact line at the heater wall is shown in Fig. 4(b). Immediately after step reduction in gravity (t=0 s) the contact line started to rise along the heater wall. Due to the low damping of the system (low Ohnesorge number) the contact line showed an overshoot compared to the final equilibrium position, which would be reached at isothermal conditions. The overshoot was followed by a viscous damped oscillation of the contact line.

During the contact line movement the dynamic contact angle was influenced by viscous forces (expressed by the capillary number) as well as by the convective flow caused by the Marangoni convection. Due to high contact line velocities and low temperature differences the viscous forces were dominant in the beginning. With increasing time the Marangoni convection gained influence and affected the flow behavior of the contact line, whereas the capillary forces decreased.

As outlined above, due to the evaluation of the contact angle at a certain distance r_l, the initial contact angle was larger than zero and took on a value of about γ_{dl}=13.3°. Then, the onset of Marangoni convection caused an overall increase of the dynamic contact angle, as shown in Fig. 5.

A more detailed view reveals that the dynamic contact angle oscillated around a certain increasing curve, see Fig. 5. This oscillation reflects the behavior of the contact line. More precisely, the apparent dynamic contact angle increased with increasing contact line velocity in the case of advancing contact line motion, whereas it decreased with increasing contact line motion for receding contact line motion. For a contact line velocity equals to zero the contact angle returned to the static contact angle. In the present study the continuously increasing Marangoni convection caused a continuously changing apparent static contact angle. The enumeration of the data points in Fig. 5 labels the apparent static contact angle at the turning points of the contact line oscillation.

Figure 6 summarizes the results of the performed experi-

TABLE IV. Scaling and dimensionless numbers for the numerical simulations. L/U is the characteristic time scale.

ϑ_u (°C)	45	55	65
L (m)		0.0188	
U (m/s)	0.0706	0.0925	0.112
L/U (s)	0.266	0.203	0.167
Pr $(-)$		9.86	
Oh $(-)$		9.27×10^{-4}	
Re $(-)$	3482	4562	5527
We $(-)$	10.4	17.9	26.2
We$_M$ $(-)$	59.0	67.5	74.3

ments. The figure shows the mean apparent dynamic contact angle at the end of the respective experiments versus We/We$_M$.

To derive a quantative relation for this dependence, we use a power law ansatz of the form

$$\gamma_{\text{shift}} = \alpha \left(\frac{\text{We}}{\text{We}_M} \right)^{\beta}. \tag{19}$$

Following and anticipating the discussion in Sec. IV, we fixed the value of $\beta = 0.75$ and fitted solely α. Together with Eq. (18) this resulted in the relation

$$\gamma_{\text{dl}} = 13.3\,^{\circ} + 59\,^{\circ} \left(\frac{\text{We}}{\text{We}_M} \right)^{3/4} \tag{20}$$

to a very good agreement.

IV. NUMERICAL SIMULATION WITH NAVIER

In this section we report on the computational results concerning the enlargement of the apparent contact angle obtained by the software NAVIER. Since we are only interested in the dependency of the apparent contact angle on nonisothermal conditions, the dynamic reorientation behavior of the free surface is of minor interest in this case. Thus, we simplify the situation by considering an annular gap in the absence of external forces, starting from the (isothermal) $0g$ equilibrium configuration.

A. Numerical methods

The flow solver NAVIER is a finite element based method on unstructured triangular grids for the simulation of transient, incompressible flows, see Ref. 14. The Taylor–Hood element (piecewise quadratic functions for the velocity and piecewise linear functions for the pressure) has been used. We used the version for axially symmetric flows.

The motion of a free surface is computed using a sharp interface model with arbitrary Lagrangian–Eulerian coordinates. More precisely, the computational domain coincides with the liquid domain, while the interface is given by the corresponding part of the boundary of the liquid domain. To this end, after each time step the computational grid is deformed according to the movement of the liquid phase. This approach leads to a very accurate representation of the geometry.

The curvature terms are formulated in a variational way, which yields a very precise, dimensionally independent and simple-to-implement approximation of the capillary forces. The solver uses a stable time discretization that is semi-implicit with respect to the treatment of the curvature terms. This firstly allows one to choose the time step independently of the mesh size—as opposed to common "explicit" treatments of the curvature terms—and secondly decouples the computation of the geometry and the flow field. This approach has proven to be both efficient and robust. For details, see Ref. 15. NAVIER has been successfully validated by many academic as well as physical examples.

B. Numerical setup and boundary conditions

The same geometric setup as described in Sec. II A was used in the numerical simulation. Dirichlet boundary conditions for the temperature were imposed at the walls. At the outer wall, the bottom, and at the lower part of the inner wall the temperature was kept constant at $\vartheta_l = 25$ °C, which was also taken as the initial (cold) temperature of the liquid. At the upper part of the inner wall, where the cartridge heater was located, the temperature was raised linearly in time until it reached some maximum value ϑ_u at the end of the numerical experiment, 5 s (in physical time) after the temperature started to rise. The value of ϑ_u was varied in different simulations. The dimensionless numbers for the simulations are
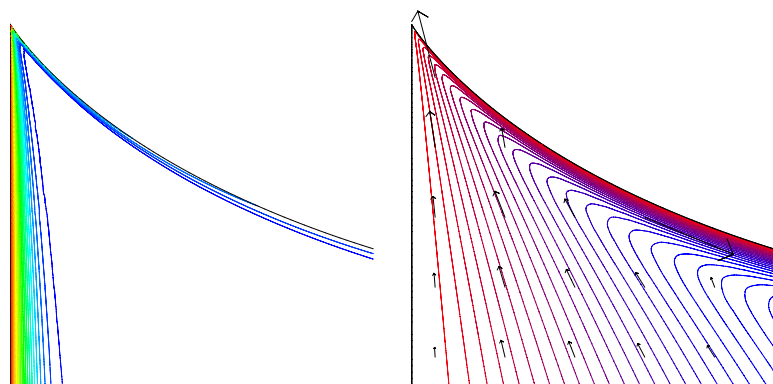

FIG. 7. (Color online) Isolines of temperature (left) and velocity vectors and streamlines (right) in the meniscus. The temperature varies from $\vartheta_l = 25$ °C in the bulk of the liquid to $\vartheta_u = 65$ °C at the heater wall. Numerical simulation with $\gamma_s = 15°$ at the end of the simulation time.
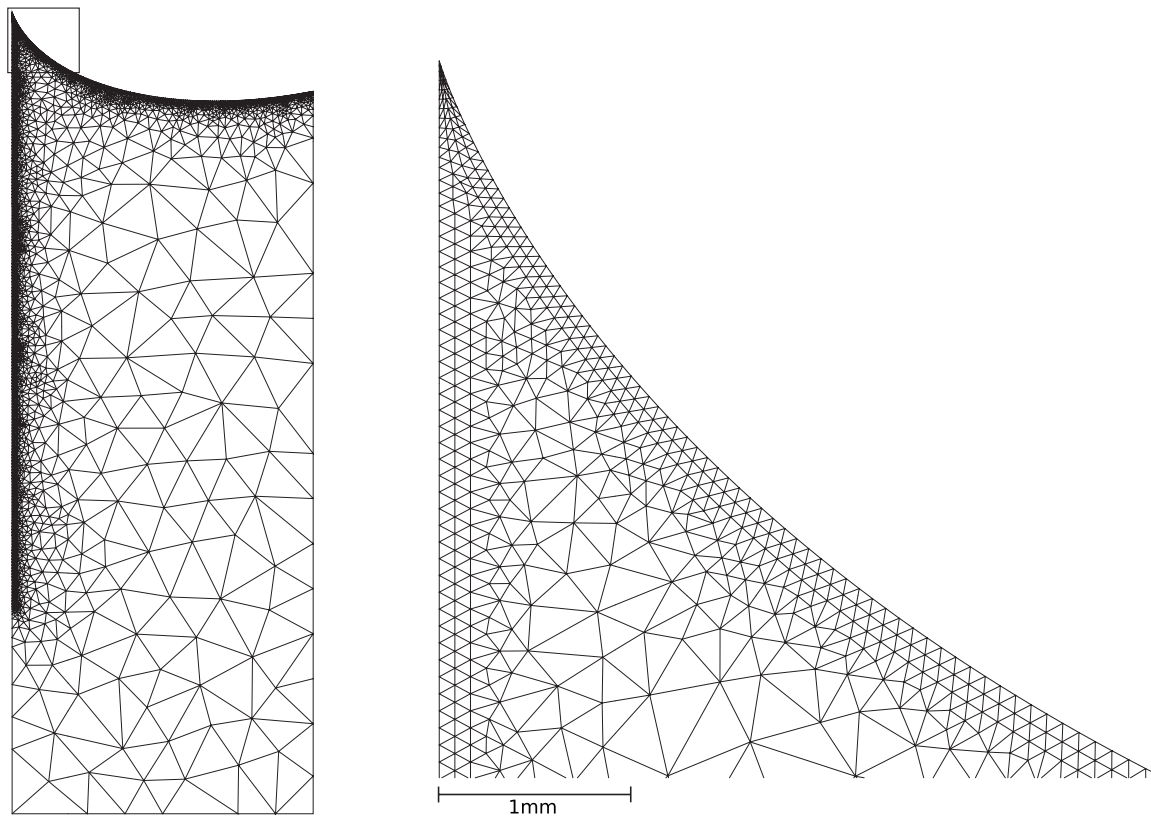
FIG. 8. Computational grid with a closeup near the contact line. The computational grid had around 6700 triangles.

given in Table IV. The gas-liquid phase boundary was assumed to be adiabatic.

For the flow field, a no slip boundary condition was imposed at the walls (except close to the contact line, see Secs. II B and IV C). At the free surface, the stress as given in Eq. (5) was prescribed. As initial conditions for the flow field and the geometry, we started with the isothermal equilibrium configuration: the velocity was set to zero, the free surface was set to the 0 g configuration, as calculated by solving the Young–Laplace equation (17) with the Bond number set to zero. In order to be sure to start in the equilibrium, the simulation was kept running in the initial state for some time before switching on the heater to allow any residual velocities arising from perturbations in the initial conditions to settle down.

All data, geometry, as well as boundary and initial conditions are axially symmetric. Since the flow is laminar, we assumed the solution to respect this symmetry, that is, the azimuthal derivatives of all quantities involved, as well as the azimuthal component of the velocity were assumed to vanish.

It might be noteworthy that the numerical solution features sharp thermal boundary layers close to the cartridge heater and even more pronounced at the phase boundary, see Fig. 7. The resolution of these layers with a sufficiently fine mesh in these regions was found to be mandatory to get correct results. A typical computational grid is shown in Fig. 8. At the heater and the liquid surface, the computational grid

has been generated by a self-written program adapted to the geometry. The coarse grid in the interior of the liquid domain has been completed using the grid generator TRIANGLE by Shewchuk, see Ref. 16. The computational grid had around 6700 triangles which results in around 28 000 degrees of freedom for the velocity, 14 000 degrees of freedom for the temperature, and 3700 degrees of freedom for the pressure.

A simple time step control was used to reduce the overall numerical effort. The actual time step sizes varied between 1.3×10^{-3} and 1.3×10^{-2} in dimensionless units.
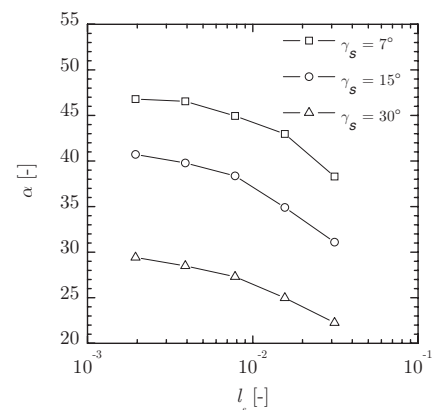

FIG. 9. α vs l_s, with α resulting from the best fit using the ansatz [Eq. (19)] with a fixed value of $\beta = 0.75$ for $\gamma_s = 15°$ and $\vartheta_u = 65$ °C.

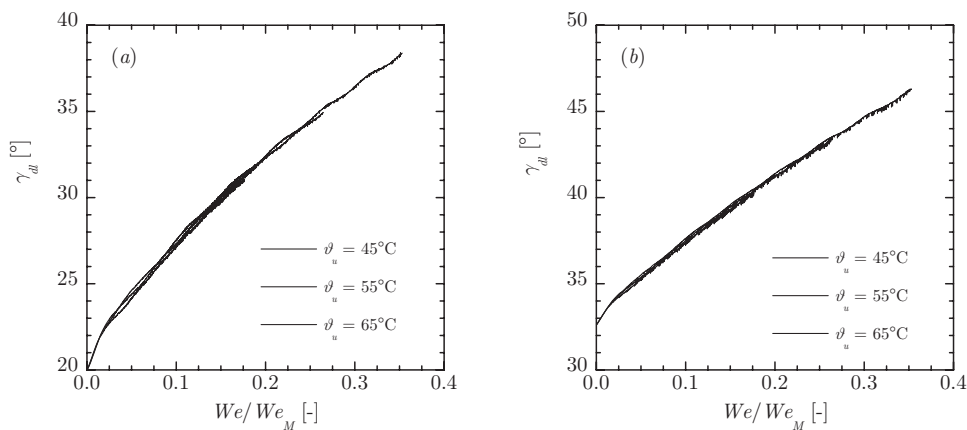FIG. 10. γ_{dl} vs We/We$_M$ for $\gamma_s = 15°$ (a) and $\gamma_s = 30°$ (b) for different maximum temperatures. The longer plots correspond to the higher temperature ϑ_u at the end of the simulation.

C. Boundary conditions at the contact line

As discussed in Sec. II B, the kinematic boundary condition (4) is in contradiction to the no slip boundary condition at the wall for a moving contact line. Therefore, the no slip boundary condition was relaxed close to the contact line in the following way: A slip boundary condition (i.e., zero normal flux and zero tangential stress) was imposed within a tiny region below the contact line. We denote the width of this region by l_s. In order to test the influence of this parameter, several simulations have been performed with varying l_s. The parameter α of the power law ansatz [Eq. (19)] has been calculated in the same way as described in Sec. IV E below, using a fixed value of $\beta = 0.75$ for the fit. Figure 9 shows that the enlargement of the apparent contact angle gets stronger for smaller values of l_s, with a certain saturation in the vicinity of $l_s = 2 \times 10^{-3}$ in dimensionless length. Thus, l_s has been fixed to this value for the rest of the simulations.

As boundary condition for the shape of the the free surface, a fixed static contact angle γ_s was prescribed at the inner wall. More involved models for a dynamic contact angle generally require additional parameters that are not known *a priori*. The need to adapt these parameters would spoil the goal of our investigation to observe the behavior of the numerical simulation with respect to the apparent contact angle. Note also that we skipped the reorientation in the simulation and started in the 0g equilibrium configuration instead. In this case, the contact line does not move besides a slight recede during the simulation. A model for a dynamic contact angle is therefore not needed.

Since our numerical methods work with a sharp interface model, we cannot cope with a contact angle of 0°, i.e., with a full wetting liquid, directly. Instead, we compared runs with static contact angles varying from 50° down to 7°.

D. Data evaluation

As described in Sec. II B we define the apparent contact angle γ_{dl} as the slope of the free surface at a distant of $r_l = 0.14$ mm from the inner wall and the enlargement of this angle compared to the isothermal equilibrium shape γ_{shift} as in Eq. (18). In order to establish a relation for γ_{shift} as a function of γ_s and the nonisothermal condition expressed by We/We$_M = \sigma_T \Theta / \sigma$ we used the power law ansatz from Eq. (19),
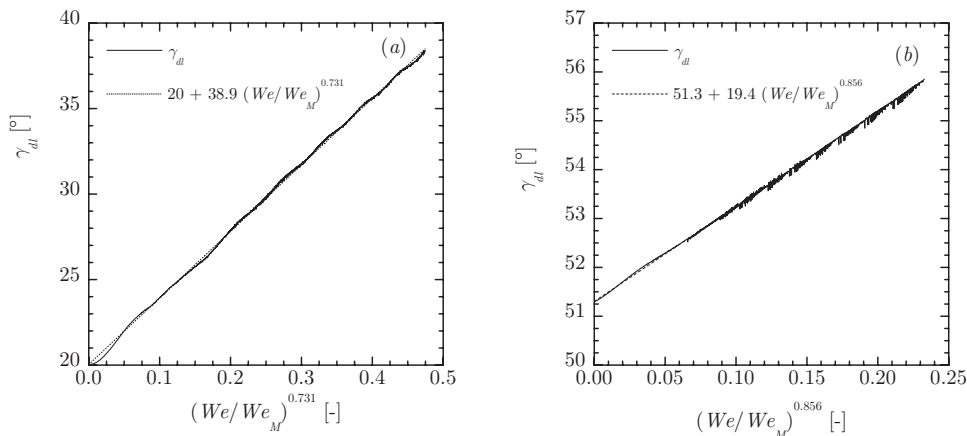

FIG. 11. Best fit for α and β using the ansatz [Eq. (19)] for $\vartheta_u = 65$ °C, $\gamma_s = 15°$ (a) and $\vartheta_u = 45$ °C, $\gamma_s = 50°$ (b).
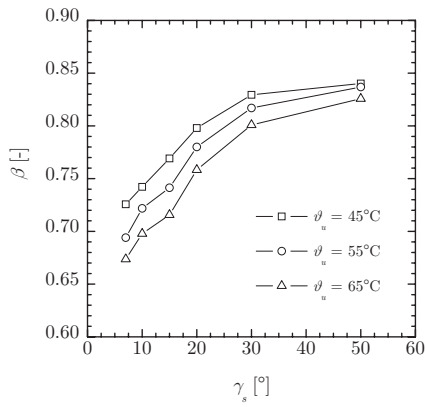
FIG. 12. Values of the exponent β as a result of the best fit for the ansatz [Eq. (19)].

FIG. 14. α vs γ_s, with α resulting from the best fit using the ansatz [Eq. (19)] with a fixed value of $\beta=0.75$.

$$\gamma_{\text{shift}} = \alpha \left(\frac{\text{We}}{\text{We}_M} \right)^{\beta},$$

where now α and β may depend on γ_s.

E. Results

Since the inner wall temperature raised in time, we got a time dependent value for Θ and thus for We/We_M, see Eq. (16). Thus each numerical experiment delivered one relation of γ_{dl} versus We/We_M. Figure 10 shows that the curves for different values of ϑ_u match very well for each value of γ_s.

To acquire values for α and β, in a first approach a least squares fit for ansatz [Eq. (19)] was computed individually for each run. Figure 11 shows two typical results of this fit for two different runs. The fit matches very well, so the power law ansatz seemed to be justified. The exponents β from the fits for all the runs are shown in Fig. 12. The value of this exponent is almost constant and varies only between 0.67 and 0.84, with a tendency of a smaller β for smaller γ_s and bigger ϑ_u, that is, for the experiments where the overall change in γ_{dl} is most pronounced. Choosing a constant value of $\beta=0.75$ thus seemed to be appropriate.

In a second approach, now α was solely fitted for ansatz [Eq. (19)] individually for each run, with the fixed value of
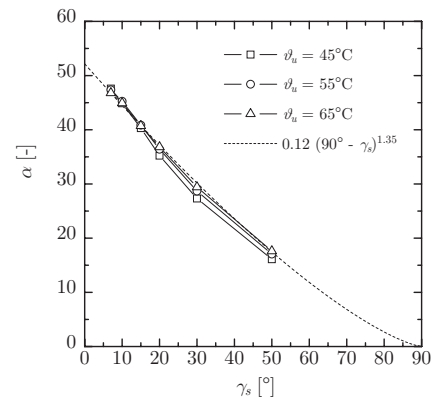
$\beta=0.75$, see Fig. 13. Note that Fig. 13(b) shows the worst case, the run, where originally the discrepancy of β from the value of 0.75 was the largest. Nevertheless, the data match quite well.

Figure 14 shows α as a result from the fit with the fixed value of $\beta=0.75$ versus γ_s. Again, the curves for different values of ϑ_u agree well. As one should expect, α clearly decreases with larger γ_s. Note that for $\gamma_s=90°$ the impact of the nonisothermal conditions on γ_{dl} vanishes.

A further power law ansatz for α as a function of γ_s yielded

$$\alpha = 0.12(90° - \gamma_s)^{1.35}. \tag{21}$$

The upshot of all data analysis for γ_{shift} is therefore

$$\gamma_{\text{shift}} = 0.12(90° - \gamma_s)^{1.35} \left(\frac{\text{We}}{\text{We}_M} \right)^{0.75}. \tag{22}$$

Extrapolating to the case of a full wetting fluid, characterized by $\gamma_s=0$, is then

$$\gamma_{\text{shift}} = 52.0° \left(\frac{\text{We}}{\text{We}_M} \right)^{0.75}. \tag{23}$$
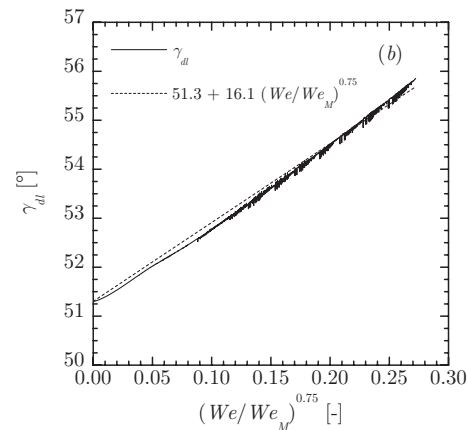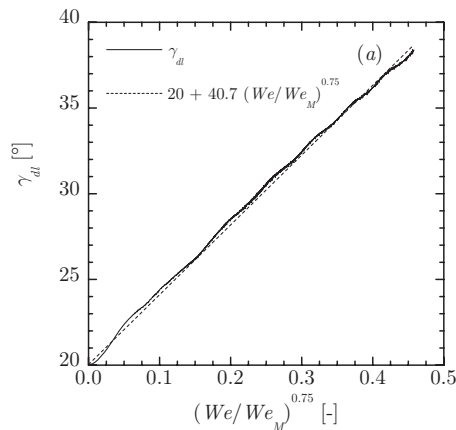

FIG. 13. Best fit for α using the ansatz [Eq. (19)] with fixed value $\beta=0.75$ for $\vartheta_u=65\ °\text{C}$, $\gamma_s=15°$ (a) and $\vartheta_u=45\ °\text{C}$, $\gamma_s=50°$ (b).
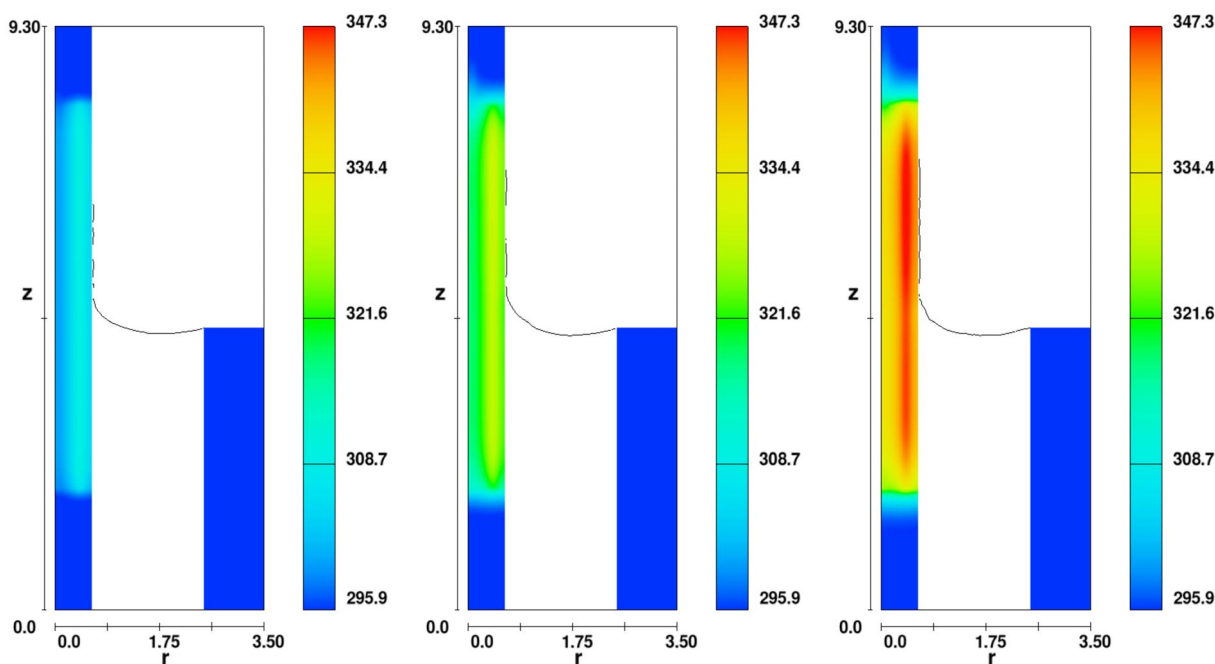
FIG. 15. (Color online) Temperature distribution in heater element in K; sequence of FLOW-3D frames at $t = 1$ s, $t = 3$ s, $t = 5$ s.

V. ASSESSMENT WITH THE COMMERCIAL FLOW-3D SOFTWARE

In space industry the commercial software tool FLOW-3D is frequently used for solving problems concerning the propellant behavior under microgravity conditions due to its functionality, effectiveness, and reliable reproduction of physical features, in general. A crucial issue is the validation and benchmarking of commercial tools such as FLOW-3D. Thus, we complemented our experimental and numerical investigation by simulations performed by FLOW-3D.

The following physical and numerical conditions were applied:

- A static 0° contact angle was prescribed.
- Any influences from the gas phase, including heat exchange and evaporation effects, were neglected.
- Laminar viscous flow was applied.
- The cartridge heater has been fully modeled prescribing the heating power.
- A no-slip condition holds at the wall/liquid interface.
- The numerical model used grids of 140×372 and 280×744 cells.

As a representative example, the case with 200 W heating power was simulated. Figure 15 shows the temperature distribution inside the heater element and Fig. 16 the corresponding liquid temperature obtained by FLOW-3D.

The heater temperature profile was monitored at the same locations as defined in the experiment. A comparison of the temperature (experiment versus FLOW-3D solution) for the average of the values from Tc3 and Tc4 is shown in Fig. 17(a). The temperature history profile is close to the experimental measurement. Thus it can be concluded that the thermal boundary conditions at the wall-liquid interface from the experiment were well reproduced in the numerical simulation.

The cell sizes in the computational grid were 0.25 mm for the coarse grid and 0.125 mm for the fine grid. Note that this is already much finer than the meshes used for real applications in the industry. But still, it is too coarse to evaluate the apparent contact angle at r_l as in the previous sections. Therefore the slope of the free surface between the third and the fourth cell was taken to be the apparent contact angle γ_{dl} for the coarse grid and the slope between the ninth and the tenth cell was taken for the fine grid.

A best fit for γ_{dl} using the power law ansatz [Eq. (19)] with value of $\beta = 0.75$ yielded

$$\gamma_{dl} = 13.3\,° + 28.7\,° \left(\frac{We}{We_M} \right)^{0.75} \tag{24}$$

for the grid with 140×372 cells. In order to investigate the convergence behavior of the numerical simulation, a second analysis was carried out with a grid of half the cell size (280×744 grid). Using this grid, the fit for γ_{dl} yields

$$\gamma_{dl} = 13.3\,° + 39.4\,° \left(\frac{We}{We_M} \right)^{0.75}. \tag{25}$$

The contact angle values become larger using the finer grid. The measured contact angle with respect to time is shown in Fig. 17(b) for the coarse and the fine grid calculation. Due to the representation of the free surface within the volume of fluid (VOF) method of FLOW-3D, the curve of γ_{shift} appears to be rather wiggly. The fit shows that obviously the numerical data underestimated the influence of the dynamic contact angle by about 55% for the coarse grid calculation. In the case of a finer grid of half the cell size this value reduced to about 40% for this test example.
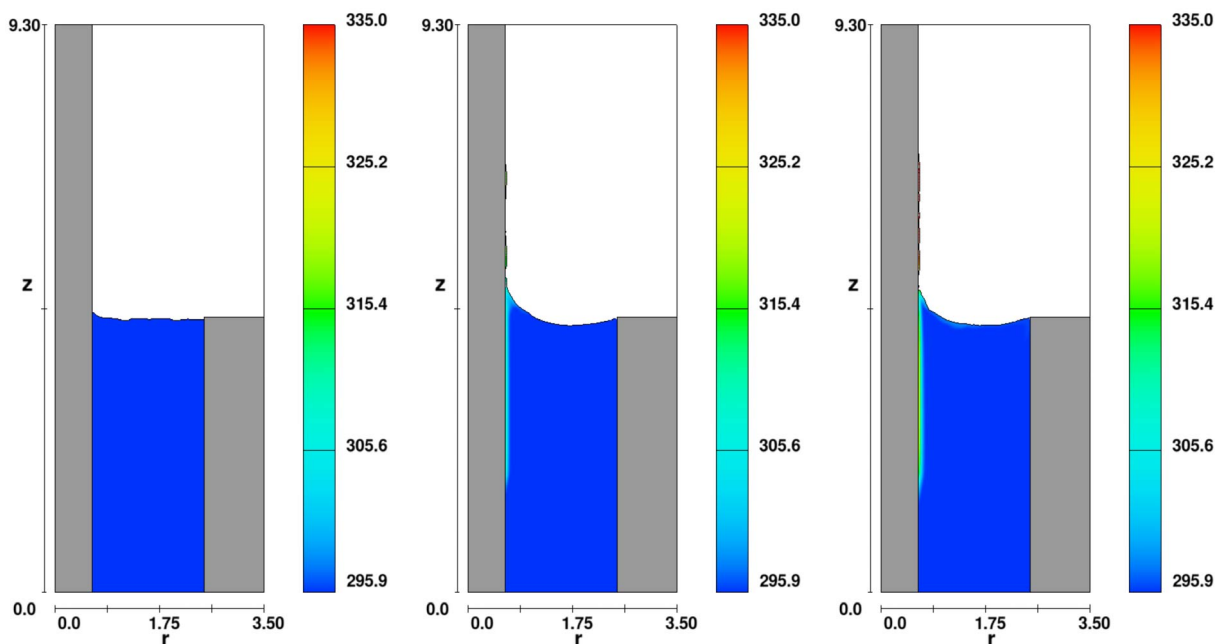
FIG. 16. (Color online) Temperature distribution in liquid in K; frames at $t=0$ s, $t=3$ s, $t=5$ s, 140×372 grid.

VI. CONCLUSION

Experiments and numerical calculations were performed to investigate the effect of Marangoni convection on the dynamic contact angle and on the dynamic behavior of the free liquid interface at compensated gravity conditions. In the experiments, microgravity conditions were obtained after the release of a drop capsule in the drop tower facility Bremen.

Thermocapillary flows were generated in an annular gap partly filled with a high Prandtl number (≈ 10) fluid. The fluid was heated by a cylindrical cartridge heater at the center. The relevant dimensionless parameter to characterize this system is the ratio

$$\frac{\text{We}}{\text{We}_M} = \frac{\sigma_T \Theta}{\sigma}$$

of Weber number We and thermocapillary Weber number We_M, where Θ is the temperature difference between the heater wall and the liquid. The supply of constant heating power ensured a linear increase of temperature difference during the experiment time. The heating power was varied between 0 and 200 W, resulting in an increase of the heater temperature within the experiment time between 0 and 44.4 K. Thus the thermocapillary Weber number was varied in the range of 0–0.34.

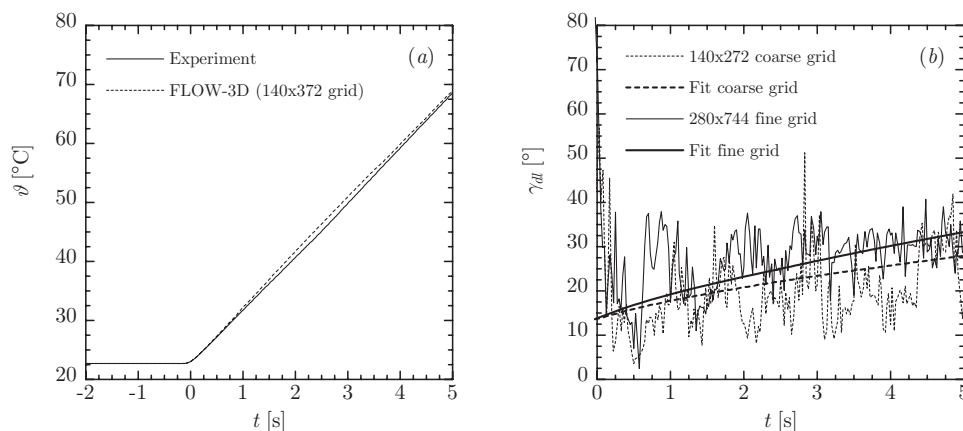The measured data show that the Marangoni convection

FIG. 17. Numerical simulations with FLOW-3D. (a) Temperature history of upper temperature sensor location $(Tc3+Tc4)/2$. Comparison of experiment and numerical solutions with the 140×372 grid. (b) contact angle γ_{dl} and fit according to power law (140×372 and 280×744 grid) as given in Eqs. (24) and (25).
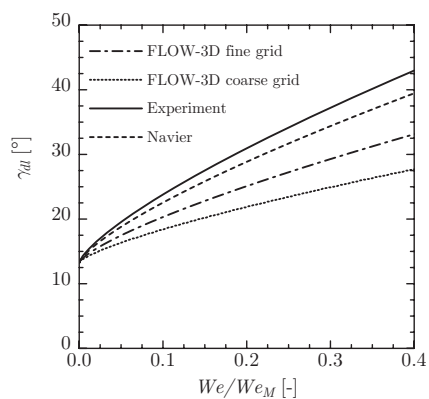
FIG. 18. Power law for the apparent contact angle for full wetting fluids as a function of We/We$_M$. Comparison between the results from experiments and from numerical simulations with NAVIER and FLOW-3D.

caused an increase of the apparent dynamic contact angle. The numerical simulations using the flow solver NAVIER turned out to reproduce the results from the experiments quite well even with the simple model of a static contact angle, provided the computational grid was fine enough to resolve the thermal boundary layers. This suggests that the enlargement of the apparent contact angle is due to thermocapillary effects at the surface and need not to be explained by other effects directly at the contact line.

The enlargement γ_{shift} of the apparent contact angle as a function of the ratio $\sigma_T \Theta / \sigma$ of Weber number We and thermocapillary Weber number We$_M$ has been successfully fitted from the experimental and numerical data by a power law. For the experiments, this fit yielded

$$\gamma_{\text{shift}} = 59.0\,^\circ \left(\frac{\text{We}}{\text{We}_M} \right)^{3/4}.$$

For the numerical simulations, the static contact angle γ_s was varied, resulting in

$$\gamma_{\text{shift}} = 0.12(90\,^\circ - \gamma_s)^{1.35} \left(\frac{\text{We}}{\text{We}_M} \right)^{3/4}.$$

Extrapolating this result to the full wetting case $\gamma_s = 0$ results in

$$\gamma_{\text{shift}} = 52.0\,^\circ \left(\frac{\text{We}}{\text{We}_M} \right)^{3/4},$$

which is slightly below the experimental findings, see Fig. 18.

This law may be helpful in estimating the accuracy of numerical tools with respect to Marangoni convection. Moreover, it can be used as a *subgrid model*, when the grid cannot resolve the boundary layers, which is usually the case in industrially relevant situations.

For instance, the commercial software FLOW-3D is frequently used for these kind of problems in space industry due to its functionality, effectiveness, and reliable reproduction of physical features, in general. However, numerical simulations performed by FLOW-3D tend to strongly underestimate the influence of Marangoni convection on the enlargement of the apparent contact angle. This effect is strongly mesh dependent, of course being more pronounced on coarser meshes. Since the industrially relevant geometries are of three dimensional nature, having length scales of meters, meshes are usually much coarser than the ones used in the present study for a simple two dimensional geometry.

An adaptation of the code's current contact angle model as a function of the temperature gradient may therefore be necessary, if accurate results concerning the location of the temperature dependent interface under microgravity are required. Our findings may provide such a kind of subgrid contact model.

ACKNOWLEDGMENTS

[1]M. Jäger, "Launching Rosetta—The demonstration of ARIANE 5 upper stage versatile capabilities," *55th International Astronautical Congress*, Vancouver, Quebec, 4–8 October 2004 (AIAA, Reston, 2004), Paper IAC-04-V.3.01, URL: http://www.aiaa.org/content.cfm?pageid=406&gTable =Paper&gID=42813.

[2]J. Gerstmann, M. Michaelis, and M. E. Dreyer, "Capillary driven oscillations of a free liquid interface under non-isothermal conditions," Proc. Appl. Math. Mech. **4**, 436 (2004).

[3]P. Ehrhard and S. H. Davis, "Non-isothermal spreading of liquid drops on horizontal plates," J. Fluid Mech. **229**, 365 (1991).

[4]P. Ehrhard, "Experiments on isothermal and non-isothermal spreading," J. Fluid Mech. **257**, 463 (1993).

[5]D. M. Anderson and S. H. Davis, "The spreading of volatile liquid droplets on heated surfaces," Phys. Fluids **7**, 248 (1995).

[6]R. Krahl and E. Bänsch, "Impact of Marangoni effects on the apparent contact angle—A numerical investigation," Microgravity Sci. Technol. **17**, 39 (2005).

[7]M. Michaelis, M. E. Dreyer, and H. J. Rath, "Experimental investigation of the liquid interface reorientation upon step reduction in gravity," Ann. N.Y. Acad. Sci., **974**, 246 (2002).

[8]M. E. Dreyer, *Free Surface Flows under Compensated Gravity Conditions*, of Springer Tracts in Modern Physics, Vol. 221 (Springer, Berlin, 2007).

[9]Y. Kamotani, S. Ostrach, and J. Masud, "Microgravity experiments and analysis of oscillatory thermocapillary flows in cylindrical containers," J. Fluid Mech. **410**, 211 (2000).

[10]P.-G. de Gennes, "Wetting: Statics and dynamics," Rev. Mod. Phys. **57**, 827 (1985).

[11]H. Lamb, *Hydrodynamics* (Dover, New York, 1945).

[12]S. Ostrach, "Low-gravity fluid flows," Annu. Rev. Fluid Mech. **14**, 313 (1982).

[13]Y. Kamotani, A. Chang, and S. Ostrach, "Effects of heating mode on steady axisymmetric thermocapillary flows in microgravity," J. Heat Transfer **118**, 191 (1996).

[14]E. Bänsch, "Simulation of instationary, incompressible flows," Acta Math. Univ. Comen. **67**, 101 (1998).

[15]E. Bänsch, "Finite element discretization of the Navier-Stokes equations with a free capillary surface," Numer. Math. **88**, 203 (2001).

[16]J. R. Shewchuk, "Triangle: Engineering a 2d quality mesh generator and delaunay triangulator," Lect. Notes Comput. Sci. **1148**, 203 (1996).